Ignition probability of a partially premixed burner using LES

Lucas Esclapez [a,b,*], Eleonore Riber [a], Bénédicte Cuenot [a]

[a] *CERFACS, 42 Avenue G. Coriolis, 31057 Toulouse Cedex 01, France*
[b] *SNECMA Villaroche, Rond-Point René Ravaud-Réau, 77550 Moissy Cramayel, France*

Abstract

To comply with stringent pollutant emission regulation, low-emission aeronautical gas turbines rely on lean premixed combustion. Such technology raises the issue of ensuring a reliable ignition since the combustor operates closer to blow-off. Ignition is however known as a stochastic phenomenon, associated to various sources of system variability. These variabilities and their impact on the success or failure of ignition are still not fully understood. In this paper, Large Eddy Simulation (LES) of laser ignition sequences in an academic swirled turbulent partially premixed burner are performed to obtain statistical information at three selected ignition locations representative of the various ignition scenarios observed. The velocity and mixing fields are first validated against measurements to eliminate uncertainty associated with the non-reacting flow. LES is then shown to recover the ignition statistical behavior and probability for the selected ignition locations. Moreover, LES analysis allows to identify the various mechanisms that drive ignition failure or success. Statistics of flame displacement speed are used to demonstrate the effect of curvature and stretch in regions of intense turbulence and the impact of partial premixing on the ignition process.
© 2014 The Combustion Institute. Published by Elsevier Inc. All rights reserved.

Keywords: Large eddy simulation; Ignition; Turbulent partially premixed flame

1. Introduction

In the domain of aeronautical propulsion, the recent emphasis put on lean combustion for its promising results regarding pollutant emission gives rise to concerns about the capability to safely and rapidly ignite the combustion chamber.

During the last decade, both experiment and numerical simulations have allowed to identify the main ignition mechanisms in complex flow configurations. The ignition process in a combustion chamber may be decomposed in a series of successive steps from the formation of a small flame kernel to the ignition of the whole chamber [1]. Ignition is triggered by the deposit of energy from a spark plug or a laser beam, that creates a very high pressure and temperature plasma close to the electrodes [2] or the laser-induced breakdown region [3] respectively. In a first step this plasma cools down and generates a small flame

* Corresponding author at: CERFACS, CFD Team, 42 Avenue G. Coriolis, 31057 Toulouse Cedex 01, France. Fax: +33 (0)5 61 19 30 00.

E-mail address: esclapez@cerfacs.fr (L. Esclapez).

kernel. The second step is relative to the transition of the small kernel to a fully turbulent propagating flame. Finally the flame propagates and stabilizes at the vicinity of the injection system to reach a statistically steady-state. In real combustors having multiple injectors, these three phases are followed by a fourth step where the flame propagates from one injector to the other.

The three first phases have been studied experimentally in gaseous premixed [4,5], non-premixed [6] and two-phase [7,8] flow conditions in academic burners. These studies have demonstrated the statistical nature of ignition due to ignition system variability, local mixture and aerodynamic fluctuations, or global blow-off events [9]. As a consequence, ignition capability is usually characterized with ignition probability maps [4,5] related to local flow properties in combination with ignition scenarios [6] accounting for the flow variability during the second and third steps.

Promoted by the advances in computational power, several numerical investigations of single burner ignition have been recently conducted, mainly using Large Eddy Simulation (LES) because of the transient nature of the ignition process. LES ignition sequences of single phase turbulent jet [10] or turbulent recirculating flows [11,12] and two-phase turbulent recirculating flows [13,14] have demonstrated that the transient behavior of the flame kernel is mainly driven by the large scale flow structures. However, none of these works has extensively used LES to provide statistics, due to the associated CPU cost. Instead, methodologies for predicting the ignition probability based on non-reacting numerical solutions have been proposed. Eyssartier et al. [14] used the local flow properties and global flow patterns issued from LES to evaluate the ignition probability. This methodology has shown some limitation in capturing the mechanisms of ignition in the second and third steps where the kernel trajectory plays an important role. In a similar approach, Neophytou et al. [15] used non-reacting time-averaged fields (from either Reynolds Averaged Navier–Stokes or time-averaged LES simulations) in combination with a Lagrangian particle tracking method to compute trajectories of "flame particles", and build the ignition probability. Results obtained with this methodology give a reasonably accurate estimation of the ignition probability in several configurations but were found too dependent on user-defined parameters [15].

This work proposes to use LES of full ignition sequences to directly predict ignition probability and identify the mechanisms responsible for success or failure. The configuration is the experiment of Cordier et al. [6] where the ignition performances of an academic swirled burner were investigated. Several ignition mechanisms were identified depending on the ignition location, and are studied here with LES. The experimental

and numerical set-ups are described in Section 2. The non-reacting LES result accuracy is reported in Section 3. Section 4 provides ignition probability results and analysis of ignition sequences.

2. Configuration

2.1. Experimental set-up

The experimental burner was specifically designed to study ignition phenomena [5,6] in the European project Knowledge for Ignition and Acoustic Instabilities (KIAI). Experimental studies of the burner were conducted in both premixed and non-premixed modes at two levels of swirl intensity to investigate the impact of premixing and swirl on ignition performances. The burner is made of four major components, namely a plenum, a swirled injection system, a combustion chamber and a convergent exhaust Fig. 1. The injection system is composed of a central jet ($d = 4$ mm) nested within the annular swirl stream ($D_{in} = 9$ mm, $D_{ext} = 20$ mm) of the swirler, the latter consisting of 18 radially fed channels inclined by 45 degrees. The burner is operated in non-premixed mode where pure methane is injected in the jet. Air is first tranquilized in the cylindrical plenum before entering the swirler vanes. The combustion chamber is a square of 100 mm length by 260 mm height. A convergent exhaust ends the combustion chamber to avoid air admission induced by the swirling flow.

The experimental facility is operated at atmospheric conditions. The operating point studied in this work is characterized by an overall equivalence ratio $\phi = 0.75$, where the swirler is fed with 5.43 g/s of air and the central jet with 0.234 g/s of methane. Ignition is triggered by laser-induced breakdown allowing a non-intrusive control of the deposit location, duration and strength.

Stereo-Particle Image Velocimetry (SPIV) and Planar Laser-Induced Fluorescence (PLIF) measurements were used to characterize the initial flow field and fuel mixing. The experimental data are based on 1000 instantaneous measurements. High speed OH^* emission recording was used to track the flame during ignition.

2.2. Numerical set-up

The computational domain includes the four components of Fig. 1. The domain is discretized into a fully unstructured mesh using 22 million tetrahedral elements, with a cell size about 150 μm in the swirler and the mixing region and about 800 μm in the rest of the combustor. The axial direction is referred to as the z-axis, corresponding to the main flow direction, while the x-axis and y-axis denote the transverse directions. Space dimensions are non-dimensionalized by D_{ext}.
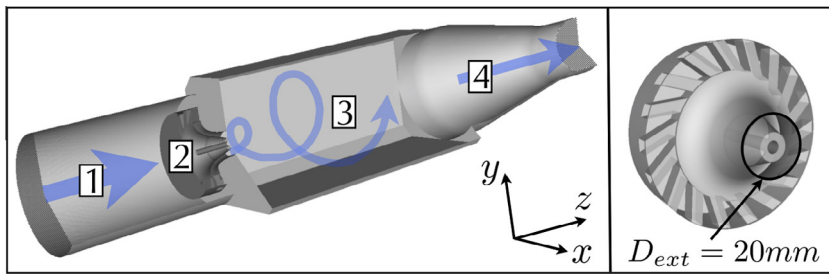
Fig. 1. Burner geometry and injection system details. Main components are: 1. Plenum, 2. Injection system, 3. Combustion chamber, 4. Convergent exit.

All simulations are performed with AVBP, an explicit cell-vertex massively-parallel code solving compressible reacting flows [16]. The equations and models used in the present study have been widely used in LES solvers and a full description can be found in the review of Gicquel et al. [17]. The third order accurate in space and time numerical scheme TTGC [18] is used. Inlet and outlet boundary conditions are treated according to the Navier–Stokes Characteristic Boundary Conditions formulation [19] and walls are considered adiabatic non-slipping. Turbulent subgrid stresses are modeled using the WALE approach [20].

Chemistry is described with the 2S_CH4_BFER scheme including 6 species, 2 reactions and Pre-Exponential constant Adjustment (PEA) to reproduce the experimental flame speed over the whole range of flammability [21]. To comply with the PEA correction, simplified transport properties are assumed with unity Lewis number for all species ($Pr = Sc_k = 0.7$ where k is the kth species). The Dynamic Thickened Flame (DTFLES) model [22,23] is employed to resolve the flame front on the LES grid and model the unresolved flame wrinkling by means of an efficiency function. In the present simulations, a moderate thickening factor will be used during the early instant following ignition, not exceeding $F \simeq 3$. The Energy Deposition (ED) model [10] is used to mimic the laser induced breakdown as a source term added to the energy equation and described with Gaussian profiles in space and time. The amount of energy deposited by the laser in the combustion chamber is measured close to 94 mJ [5]. Classically only 30% of the experimental energy deposit is considered to be transmitted to the gas due to the dissipation induced by the creation of a shock wave and radiative losses [3], so that only 30 mJ deposit energy are used in the ED model. To fully resolve the initial laminar but small scale kernel without thickening, a locally refined mesh around the ignition location (in a region of size $20\delta_{L,0}$ where $\delta_{L,0} = 0.71$ mm is the laminar flame thickness at $\phi = 0.75$) is used for the first instants of the simulation, where the cell size is reduced to $\Delta_x = \delta_{L,0}/6$. Once the flame kernel has sufficiently grown, the refined zone is suppressed and the mesh resolution corresponds to LES ($\Delta_x = 1.1\delta_{L,0}$). A study of the sensitivity of the solution to the mesh, numerical scheme and subgrid scale model has allowed to conclude that the time-averaged values are not very sensitive to none of these parameters.

At each selected location, 20 ignition sequences are computed to evaluate an ignition probability. Ignition is considered successful if the flame stabilizes at the injector. Although 20 tests make a too small sample size to provide converged statistics, it is sufficient to give a good estimate of the LES capability to reproduce such statistics. Theory of statistics indicates that a sample of size 20 results in a maximum error of about 11,2% [24].

The overall CPU cost of the study is about 1.5 M CPU hours, corresponding to 30 days of computation on an IBM Blue Gene/Q using 2048 cores.

3. Non-reacting LES validation

The cold flow topology is typical of highly swirled flows (Fig. 8(a)), where the axial adverse pressure gradient induces an Inner Recirculation Zone (IRZ) along the central axis of the burner. The IRZ is bounded in the radial direction by the Swirler Jet (SWJ) issued from the swirler and in the axial direction by the upstream stagnation point resulting from the meeting of the IRZ and central jet flows. A Corner Recirculation Zone (CRZ) is also present between the SWJ and the combustion chamber walls. Finally, strong shear layers are located between both the IRZ and the SWJ and between the CRZ and the SWJ.

First, the combustion chamber is fueled during 1.5 s (i.e. 3 residence times). Then, statistically stationary LES velocity and mixing fields are obtained by averaging during 150 ms. The accuracy of LES is first evaluated by comparing experimental and numerical profiles of the first two statistical moments of velocity at 3 axial positions in the combustion chamber corresponding to $z/D_{ext} = 0.5, 1, 1.5$. Figures 2 and 3 display the

comparison for the axial velocity component. Both the swirled jet opening and central jet penetration are well reproduced. Velocity fluctuations are slightly over-predicted in the central jet region at the 1st section. The other velocity components, not reported here for the sake of concision, also show good agreement.

Numerical prediction of mixing is then assessed by means of equivalence ratio profiles in Fig. 4. The agreement between LES and experiment is good, except for the first profile along the central axis where LES over-predicts the equivalence ratio in the central jet, which also penetrates further in the IRZ. These discrepancies could not be explained and it is not clear if it is linked to measurement or simulation error. Both differences are detrimental to ignition in LES and may have an impact on ignition statistics. However, simulation quickly recovers experimental results downstream to the first profile so that a valid ignition probability can still be obtained from LES.

4. Ignition probability

4.1. Analysis of experimental results

The experimental ignition probability map is shown in Fig. 5 (right) featuring a first zone of low ignition probability P_{ign} at the vicinity of the injector followed downstream by an intermediate zone where P_{ign} gradually increases before reaching the maximum $P_{ign} = 1$ in a large surrounding zone. Note that the intermediate zone extends over a short distance along the central axis and an increasing axial distance when going in the radial direction. Figure 5 (left) shows the probability of finding a flammable mixture built from 100 instantaneous solutions of the cold flow LES: the strong similarity between the two fields
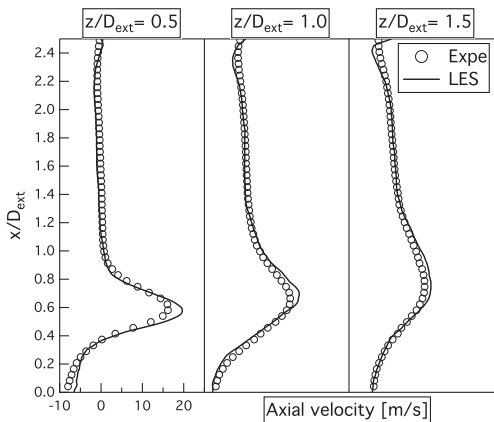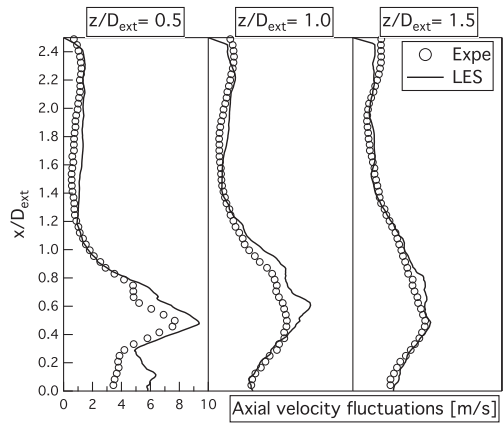

Fig. 3. LES versus experiment: axial velocity fluctuation profiles at 3 axial positions $z/D_{ext} = 0.5, 1, 1.5$.
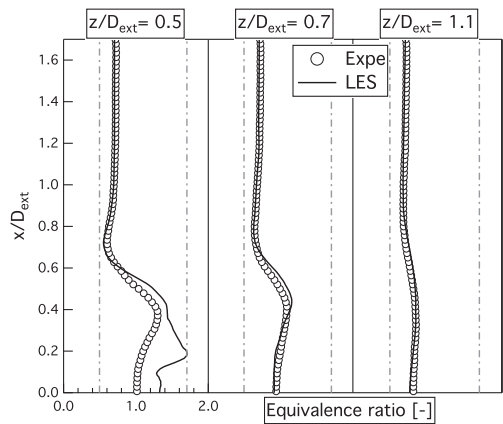

Fig. 4. LES versus experiment: time-averaged equivalence ratio profiles at 3 axial positions $z/D_{ext} = 0.5, 0.7, 1.1$. Dot-dashed lines mark the lean and rich flammability limits.

Fig. 2. LES versus experiment: time-averaged axial velocity profiles at 3 axial positions $z/D_{ext} = 0.5, 1, 1.5$.
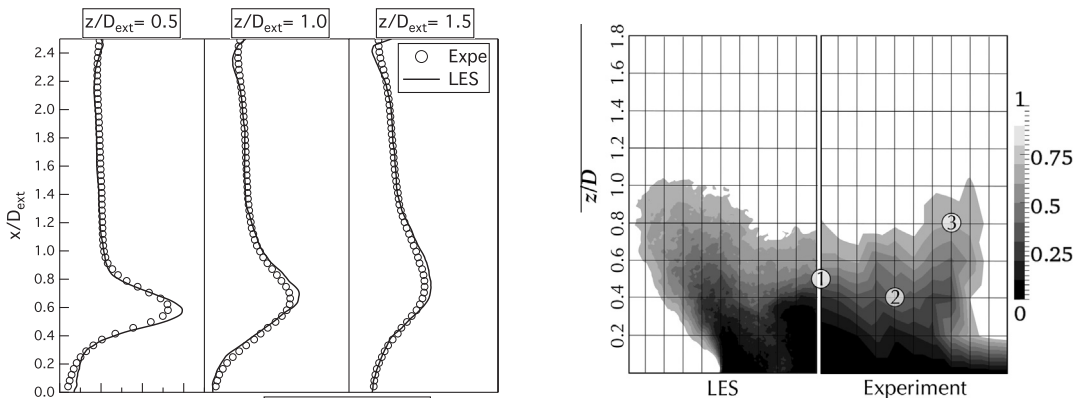

Fig. 5. Probability of finding a flammable mixture from LES (left) compared to experimental ignition probability map P_{ign} [6] (right).

shows that P_{ign} is strongly related to the local equivalence ratio. Still the exact relation between the two quantities is not clear and is the object of this work.

Based on the experimental results, three spark locations are selected to perform LES of ignition sequences. These positions are marked in Fig. 5 (right) and their coordinates are detailed in Table 1 along with the measured ignition probability. These points are selected because experiments have shown there different kernel trajectories and because they exhibit intermediate P_{ign}, indicating important stochastic behavior. Note that PT1 is not located on an experimental ignition point but lies between two points which exhibit very different values of P_{ign}. Probability density function (PDF) of mixture fraction evaluated from a temporal signal at each location is reported in Fig. 6 along with both mean and standard deviations. PDF at PT1 has a maximum likelihood near stoichiometry but the average corresponds to a rich mixture due to the spreading induced by the vicinity of the pure methane jet. The effect of intermittency of the flow is clearly visible on the PDF at PT2 with pockets of pure air or very rich mixture passing by. It induces a wide spreading of the distribution towards both rich and lean mixtures. The PDF further away from the methane jet at PT3 illustrates the good mixing properties of the burner with a small dispersion of the mixture fraction and a maximum likelihood near the lean but flammable average mixture fraction.

To evaluate more quantitatively the impact of mixture fraction on ignition, two quantities are introduced: the flammability factor F_f of Birch et al. [24] measuring the probability of finding a flammable mixture, and the flammability dispersion F'_f measuring the dispersion around stoichiometry within the flammability limits. Both are computed from the LES non-reacting flow results:

$$F_f = \int_{\xi_{lean}}^{\xi_{rich}} P(\xi) d\xi \tag{1}$$

$$F'_f = \frac{\int_{\xi_{lean}}^{\xi_{rich}} (\xi - \xi_{st}) P(\xi) d\xi}{F_f} \tag{2}$$

where $P(\xi)$ is the PDF of mixture fraction, and ξ_{lean}, ξ_{rich} and ξ_{st} are the lean and rich flammability limits and stoichiometric mixture fractions respectively (shown in Fig. 6). Flammability factors and flammability dispersion reported in Table 2 show that PT1 and PT3 have a comparable high
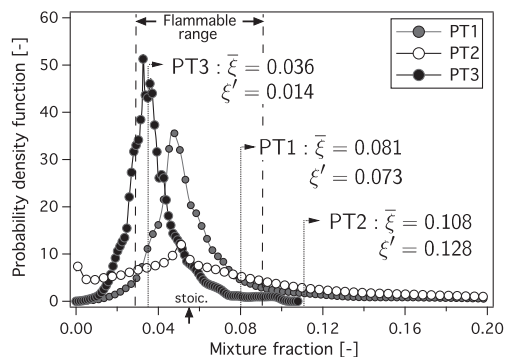

Fig. 6. PDF of mixture fraction at 3 ignition locations along with mean and standard deviation, evaluated from LES.

flammability factor but their flammability dispersion differs due the shape of their mixture fraction PDF. At PT2, the probability of finding a flammable mixture is much lower but the flammability dispersion is lower than at PT3. Finally, experimental ignition probability correlates well with flammability factor at PT2 and PT3 but the difference at PT1 demonstrates that other mechanisms influence the ignition process.

4.2. Results and discussion

Over the 60 ignition sequences computed, 32 result in a successful ignition of the burner. The ignition probability obtained by LES $P_{ign,LES}$ and reported in Table 2 compares well with the experimental P_{ign} demonstrating the capability of LES to reproduce quantitatively the stochasticity of ignition.

The early instants of the flame kernel differ from one ignition location to the other but in all cases of successful ignition, the flame is found to first develop in the IRZ where the low upstream velocity enables to ignite the incoming reactants. The hot gas volume then increases, filling the whole IRZ before expanding and pushing the flame. Overall ignition is reached in less than 25 ms while all extinctions occur during the first 5 ms after ignition.

Examples of the temporal evolution of the mean pressure in the combustion chamber in case of successful ignition are reported in Fig. 7 for each ignition position. The pressure rise is similar for each position and allows to identify a kernel

Table 1
Position of the ignition locations studied in LES, corresponding flow structure and experimental ignition probability.

	z/D_{ext}	x/D_{ext}	Location	P_{ign}
PT1	0.5	0.0	IRZ	[28–70%]
PT2	0.4	0.4	Shear layer	50%
PT3	0.8	0.7	SWJ	80%

Table 2
LES prediction of ignition probability $P_{ign,LES}$ along with estimation of the flammability factor F_f and the flammability offset F'_f at the three studied ignition locations.

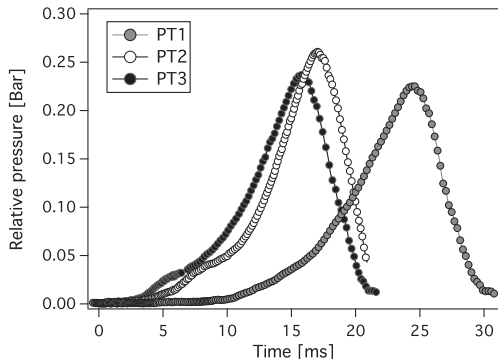|	$P_{ign,LES}$ (%)	F_f (Eq. (1))	F'_f (Eq. (2))
PT1	40	0.80	9.67×10^{-3}
PT2	48	0.46	13.41×10^{-3}
PT3	72	0.81	17.62×10^{-3}

Fig. 7. Examples of numerical temporal evolution of the mean pressure in the combustion chamber for the 3 ignition positions in case of successful ignition.

phase during which the pressure rise is negligible and a propagation phase inducing an increase of pressure in the combustion chamber. In all cases, the ignition failure only occurs during the kernel phase which is consistent with the ignition behavior observed experimentally. Ignition at PT1 is notably longer than at the other points due to the intense dislocation of the kernel while ignition at PT3 is shorter since the flame kernel enters the IRZ far downstream where the low velocity fluctuations are less detrimental to its development.

Figure 8 illustrates the different behaviors of the flame kernel motion in the x–z plane by describing the flame center of gravity trajectories during the first instants after ignition. Ignition in the lower part of the IRZ at PT1 generates a kernel close to the stagnation point, where large velocity and mixture fraction fluctuations are observed. During the first 2–4 ms, the development of the flame kernel is limited by the high aerodynamic stresses and the kernel is pushed against the methane jet. The flame features both premixed combustion in the IRZ and non-premixed combustion between the pure methane jet and the premixed IRZ flow. The kernel is highly wrinkled, local dislocations and extinctions of the flame front are frequently observed. In the few cases of success, a kernel fragment is trapped and convected downstream by the SWJ, reaching a less turbulent IRZ region where it can develop (Fig. 8(c)). This behavior is coherent with experimental observations of ignition in the lower part of the IRZ [6].

The flame kernels resulting from ignitions at PT2 span from the lower part of the IRZ to the SWJ so that a large range of equivalence ratios are encountered along the flame front. The rotating gas induces a strong bulk rotation and a radially inward motion of the kernel (Fig. 8(d)), locally submitted to high axial shear stress. The part of the flame located in the SWJ rapidly quenches due to both a lack of flammable mixture and the strong aerodynamic stresses. In the IRZ, the flame follows a development fairly similar to the flame kernel issued from ignition at PT1.

When igniting in the SWJ at PT3, the flame kernel is mainly convected in the axial direction during the first milliseconds and is wrinkled by turbulence. For all successful ignition cases, this motion is accompanied by a radially inward flame displacement (Fig. 8(b)). The kernel enters the IRZ at about $z/D_{ext} = 1.5$, where it is convected upstream towards the injector nozzle by the IRZ flow.

Two sources of ignition failure have been identified on the three ignition points: either the mixture characteristics at the energy deposit time prevents the generation of a flame kernel or turbulence/flame interactions during the kernel growth quench the flame.

Generation of flame kernel

When the mixture around the ignition location is outside the flammability limits, the ED is unable to initiate thermal runaway of the chemical
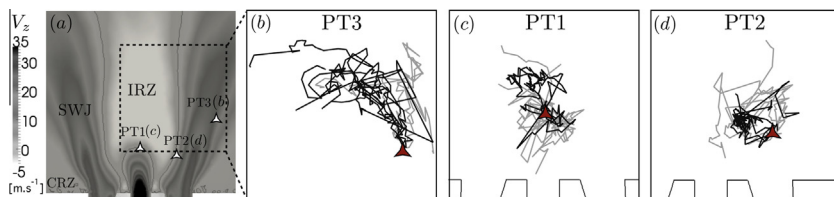

Fig. 8. Time-averaged axial velocity on an y-normal central plane along with ED locations and main flow structures (a). Trajectories of the 10 flame kernels for at PT3 (b), PT1 (c) and PT2 (d). Dark gray lines: successful ignitions, light gray lines: failed ignitions.

reactions. Either too lean mixture pockets are encountered at PT3 and PT2 because of the imperfect mixing in the SWJ, or too rich mixture is encountered at PT1 and PT2 due to the flapping of the methane jet. The high temperature pocket generated by the ED source term is dissipated below the runaway temperature in less than 0.8 ms. This effect is related to F_f reported in Table 2 which corresponds well with $P_{ign,LES}$ for PT2 and PT3 confirming the conclusion of Fig. 5. However, F_f does not give any indication about the mechanisms that lead to success or failure.

Kernel development

If a sustainable flame kernel is created, it must then survive the turbulence/flame interactions. To evaluate the impact of the flame/turbulence interaction on the flame kernel development, the flame displacement speed S_d is introduced, defined as the velocity of a progress variable isosurface relative to the gaseous velocity. In the present work, the progress variable c is the reduced temperature given by:

$$c = \frac{T - T_f}{T_{ad,st} - T_f} \qquad (3)$$

where T_f and $T_{ad,st}$ are the fresh gas temperature and the stoichiometric adiabatic temperature

respectively. Note that in a partially premixed context, where the equivalence ratio varies along and across the flame front, only this definition of the progress variable ensures $0 < c < 1$. Introducing Eq. (3) in the energy transport equation written in terms of temperature and neglecting the pressure and viscous terms, results in the following definition of S_d [25]:

$$S_d = \frac{1}{\rho C_p |\nabla T|} \left[\frac{\dot{\omega}'_T \varepsilon}{F} + \nabla(\varepsilon F \lambda \nabla T) - \nabla T \left(\rho \sum_{k=1}^{N_{spec}} C_{p,k} Y_k V_k \right) \right] \qquad (4)$$

where C_p is the mixture constant pressure heat capacity, λ is the mixture heat conductivity, $\dot{\omega}'_T$ is the heat release and $C_{p,k}$, Y_k and V_k are the constant pressure heat capacity, mass fraction and diffusion velocity of the kth species respectively. Note that the definition includes DTFLES parameters F and ε the thickening factor and the efficiency function respectively, so that the modeled flame response to strain and curvature is taken into account. S_d is oriented along the flame front normal pointing towards the fresh gases $\vec{n} = -\nabla c / |\nabla c|$. In the following, the density-weighted displacement speed $S_d^* = \rho S_d / \rho_f$ (where ρ is the local density and ρ_f is the fresh gas density) is preferred to eliminate the effect of density variation across the flame. As observed by Jenkins
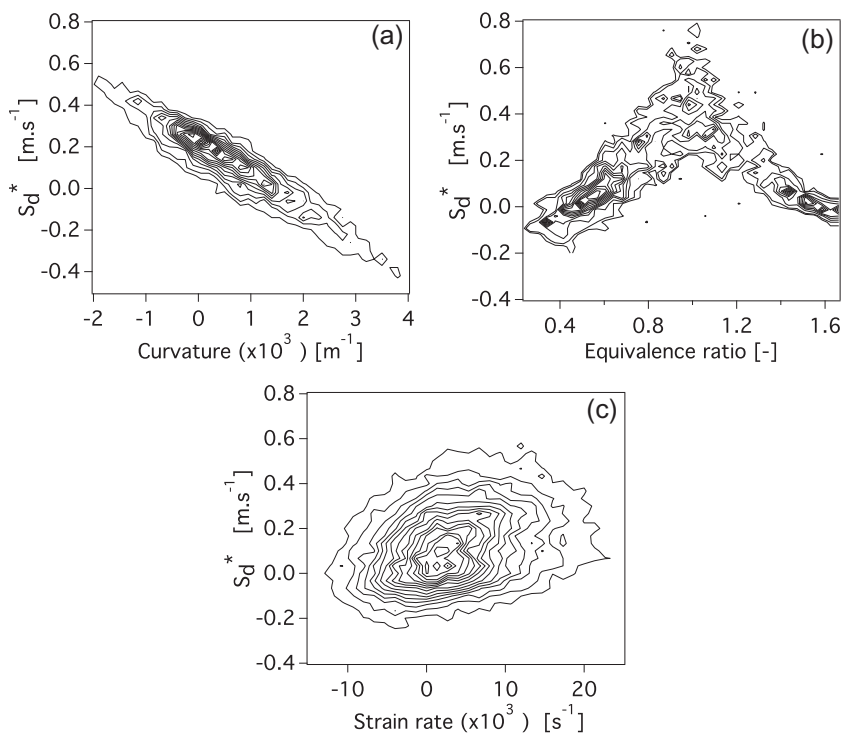

Fig. 9. Examples of joint PDF of density-weighted displacement speed S_d^* versus curvature κ (a), equivalence ratio ϕ (b) and tangential strain rate a_T (c) computed for $c = 0.3 \pm 0.05$ at $t = 0.4$ ms after ignition.

et al. [26] in Direct Numerical Simulation (DNS) of spherical flame kernel propagation in turbulent flow S_d^* is found to slightly increase across the flame front, and to be notably lower than the unstrained planar laminar flame speed $S_{l,0}$. However, S_d^* is fairly constant for iso-surfaces of c in $0.2 < c < 0.6$, and the following analysis will be focused in this range to minimize the bias introduced by the variation of S_d^*. Note that S_d^* can take negative values, that corresponds to a backward displacement of the iso-surface when the flame front is strongly thickened [27,28], usually in highly curved regions.

Examples of joint PDF of S_d^* versus equivalence ratio ϕ, curvature κ and tangential strain rate a_T are shown in Fig. 9, measured at PT3 for (a) and (c) and PT1 for (b). The negative correlation between S_d^* and κ is clearly depicted. S_d^* is found slightly below $S_{l,0}$ (0.24 m s^{-1}) due to the spherical shape of the kernel with the maximum likelihood around small positive curvature ($\sim 500 \text{ m}^{-1}$). For moderate positive or negative curvature, S_d^* keeps a positive value and for highly positive curvature S_d^* falls below zero denoting an increase of the flame thickness, which is detrimental to the kernel development as it can lead to local quenching through diffusion. This result obtained in a LES context is consistent with 2D and 3D DNS studies [26,29], and is identified as a major cause of local extinction. The dependency of S_d^* to ϕ is found to follow the laminar flame speed behavior with maximum values of S_d^* close to stoichiometry and decreasing values for both lean and rich mixtures. Finally the tangential strain rate is found slightly positively correlated with S_d^*, in accordance with DNS studies showing that for intense methane-air flame/turbulence interactions, the strain rate effect is only of secondary importance compared to the curvature effect [26].

In an attempt to discriminate successful from failed ignition, all ignition tests are gathered in a κ–ϕ map in Fig. 10. Each marker corresponds to space- and time-averaged values along the flame front ($c = 0.4 \pm 0.2$) and over the first 0.5 ms of the ignition sequence. Gray and white symbols correspond to successful and failed ignition events respectively, while circles, squares and triangles refers to ignition at PT1, PT2 and PT3 respectively. The first observation is that equivalence ratio is the major criterion impacting the success of ignition with most of the ignition successes within the flammability limits. Ignition sequences at PT1 exhibit averaged equivalence ratios outside flammability limits, which is coherent with the observations on the F_f of PT1: part of the flame encounters a very rich mixture strongly increasing the mean equivalence ratio over the flame. The distribution of successful and failed ignition events seems to indicate a dependance on curvature: the kernel survival is more probable for
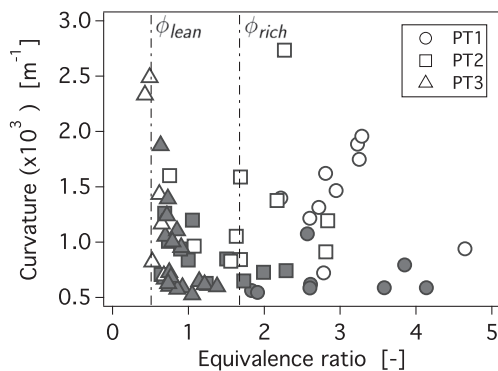

Fig. 10. Space and time-averaged values of ϕ, κ for all ignition tests in a ϕ–κ map.

low values of curvature. However, because of the averaging procedure the distinction is not perfectly clear and history effects should be taken into account to fully discriminate the impact of curvature.

5. Conclusions

Multiple LES of full ignition sequences of an academic swirled partially premixed burner have been performed to build ignition statistics at three selected locations in the combustion chamber. The LES ignition probability is found in good agreement with experiment, demonstrating the capability of LES to reproduce quantitatively the stochasticity of ignition. Common mechanisms for ignition success or failure are identified for all ignition sequences: ignition is successful if the flame kernel penetrates the IRZ and grows to a minimum size. Failure is either due to the local mixture fraction at ignition time and location that prevents the formation of a flame kernel or to a strong flame/turbulence interaction that dislocates the flame kernel and leads to quenching through a diffusion process. Using the flame displacement speed S_d^*, the effects of curvature, equivalence ratio and strain rate on the flame kernel development are identified. For ignition to be successful, the equivalence ratio should stay in the flammability limits and the mean curvature should remain as low as possible along the flame. Future work will use the present LES ignition database and the experimental ignition map to build an ignition probability model from non-reacting LES flows taking into account the history effects along kernel trajectories.

References

[1] A.H. Lefebvre, *Gas Turbine Combustion*, second ed., Taylor & Francis, 1998.

[2] R. Maly, M. Vogel, *Proc. Combust. Inst.* 17 (1978) 821–831.

[3] D. Bradley, C. Sheppard, I. Suardjaja, R. Woolley, *Combust. Flame* 138 (2004) 55–77.

[4] S. Ahmed, R. Balachandran, T. Marchione, E. Mastorakos, *Combust. Flame* 151 (2007) 366–385.

[5] M. Cordier, A. Vandel, G. Cabot, B. Renou, A. Boukhalfa, *Combust. Sci. Tech.* 185 (3) (2013) 379–407.

[6] M. Cordier, Allumage et propagation de flamme dans les écoulements fortement swirlés: études expérimentales et numériques., Ph.D. Thesis, INSA Rouen, 2013.

[7] R. Read, J. Rogerson, S. Hochgreb, in: 46th AIAA Aerospace Sciences, AIAA-2008-0956, 2008.

[8] T. Marchione, S. Ahmed, E. Mastorakos, *Combust. Flame* 156 (2009) 166–180.

[9] E. Mastorakos, *Prog. Energy Combust. Sci.* 35 (2009) 57–97.

[10] G. Lacaze, E. Richardson, T. Poinsot, *Combust. Flame* 156 (2009) 1993–2009.

[11] A. Triantafyllidis, E. Mastorakos, R. Eggels, *Combust. Flame* 156 (2009) 2328–2345.

[12] V. Subramanian, P. Domingo, L. Vervisch, *Combust. Flame* 157 (2010) 579–601.

[13] W.P. Jones, A. Tyliszczack, *Flow Turbul. Combust.* 85 (2010) 711–734.

[14] A. Eyssartier, B. Cuenot, L. Gicquel, T. Poinsot, *Combust. Flame* 160 (2013) 1191–1207.

[15] A. Neophytou, E. Richardson, E. Mastorakos, *Combust. Flame* 159 (2012) 1503–1522.

[16] L.Y.M. Gicquel, N. Gourdain, J.-F. Boussuge, et al., *C. R. Acad. Sci.* 339 (2011) 104–124.

[17] L.Y.M. Gicquel, G. Staffelbach, T.J. Poinsot, *Prog. Energy Combust. Sci.* 38 (2012) 782–817.

[18] O. Colin, M. Rudgyard, *J. Comput. Phys.* 162 (2000) 338–371.

[19] T. Poinsot, S.K. Lele, *J. Comput. Phys.* 101 (1992) 104–129.

[20] F. Nicoud, F. Ducros, *Flow Turbul. Combust.* 62 (3) (1999) 183–200.

[21] B. Franzelli, E. Riber, L.Y.M. Gicquel, T.J. Poinsot, *Combust. Flame* 159 (2) (2012) 621–637.

[22] O. Colin, F. Ducros, D. Veynante, T. Poinsot, *Phys. Fluids* 12 (7) (2000) 1843–1863.

[23] F. Charlette, D. Veynante, C. Meneveau, *Combust. Flame* 131 (2002) 159–180.

[24] M. Smith, A.D. Birch, D.R. Brown, M. Fairweather, *Proc. Combust. Inst.* 21 (1986) 1403–1408.

[25] T. Poinsot, D. Veynante, Theoretical and Numerical Combustion, Third Edition, 2011.

[26] K. Jenkins, M. Klein, N. Chakraborty, R. Cant, *Combust. Flame* 145 (2006) 415–434.

[27] I. Gran, T. Echekki, J.H. Chen, *Proc. Combust. Inst.* 26 (1996) 323–329.

[28] N. Chakraborty, R. Cant, *Combust. Flame* 137 (2004) 129–147.

[29] H. Reddy, J. Abraham, *Fuel* 103 (2013) 1090–1105.